Influence of Aortic Side Branches Involvement on Predicting Thrombosis Risk Zones in Type B Aortic Dissection: A Patient-Inspired Computational Study

Vanda Alexandra Justino Oliveira[1,2]

Supervisors: Prof. Patrick Segers[2], Prof. Paulo Fernandes[1]; **Co-Supervisors:** Gerlinde Logghe[2], Lise Gheysen[2]

[1] Instituto Superior Técnico, University of Lisbon, Portugal; [2] bioMMeda, Ghent University, Belgium.

October 2019

Abstract

Aortic dissection is defined as a tear in the aortic wall, leading to blood flow into a false lumen. Among the cardiovascular diseases, it has one of the highest mortality rates, which is also linked to thrombosis of the false lumen. For type B aortic dissection, estimation of thrombosis risk zones by analysing haemodynamic parameters is a common approach in computational studies. The aortic side branches are usually excluded from the geometries used in these studies, although these branches could explain some of the errors seen in the models. This project aims to study the influence of the involved side branches in the prediction of these thrombosis risk zones. Therefore, multiple idealized geometries with different side branches configurations were generated based on a patient CT scan and thrombus-related haemodynamic parameters were computed using computational fluid dynamics. The results show that flow patterns and haemodynamic parameters differ between geometries with and without side branches and depending on the side branches configuration, over- or underestimation of thrombosis risk zones was obtained. A smaller distance tear-branch led to larger risk zones near the tear, with this being clearer for an involved branch located closer to the aortic arch. Moreover, larger areas of thrombosis risk zones were obtained between multiple branches with the percentage of outflow via the branch being an important parameter. This study shows that the configuration of the side branches has an influence on important thrombosis-related parameters. This knowledge could help both doctors and engineers to better predict false lumen thrombosis.

Keywords: Type B Aortic Dissection, Computational Fluid Dynamics, Thrombosis, False Lumen, Aortic Side Branches

1. Introduction

Aortic Dissection (AD) is a cardiovascular disease characterized by the disruption, i.e. tear, of the intimal layer of the aortic wall. This allows blood to flow through both the normal pathway (i.e. True Lumen, TL) and an alternative pathway (i.e. False Lumen, FL). A 45.2% mortality rate has been found for AD patients up to 30 days after hospital discharge, with an incidence value of 3.5/100 000 per year [1, 2].

Cases where only the descending section of the aorta is affected are classified as Type B Aortic Dissection (TBAD) [3]. The aim of treatment in TBAD is to decrease the blood pressure in uncomplicated cases in order to prevent further dilatation and aneurysmal degradation in these cases. For complicated cases, open surgery or TEVAR is used to seal the entry-tear and promote thrombosis and aortic remodelling of the FL [4]. Lower success rates for TEVAR procedures have been found for men, patent or partially thrombosed FL and for cases with involved side branches (i.e. side branches with an origin in the FL) [5, 6]. Complete thrombosis means that there is only thrombus and no flow in the FL and is associated with the lowest post-discharge mortality [4, 5]. The absence of flow prevents a further expansion of the FL which could lead to aortic rupture.

Thrombus formation is a highly complex process which can be summarized into a combination of the formation of a platelet plug through activation of platelets, and the coagulation cascade leading to the formation of fibrin surrounding the platelet plug. The end result is a blood clot, which is also named thrombus when formed inside a blood vessel [7].

Thrombus initiation is the consequence of one or more factors of the Virchow's triad: hypercoagulability, endothelial injury and blood flow stasis [8]. In aortic diseases such as AD, the local changes in geometry lead to disturbed, turbulent blood flow with recirculation zones. These zones are characterized by low shear conditions, high oscillatory behaviour of the shear stress net direction and high residence times [8]. Under low shear conditions, fibrinogen promotes cell aggregation, increasing the local viscosity of blood. The cell aggregate will then adhere to the wall [8, 9]. On the other hand, high shear conditions can also activate platelets and faster than low shear through endothelial injury, cell lysis or a shear-induced platelet activation [9]. However, under high shear conditions, the cells do not adhere to the wall, since they require stagnation zones which are associated with low shear zones [8]. Stagnation zones are characterized by high residence times.

Computational fluid dynamics (CFD) studies are a common approach to identify thrombus-prone regions in the FL. Some studies incorporate all of the individual processes of the complex process of thrombus formation. However, other studies only focus on haemodynamic parameters and flow pattern, to re-

duce the complexity and computational time of the calculation [10–17]. The complex geometry of AD has been found to lead to highly disturbed flow with recirculation zones in the FL and with high velocity and wall shear stress (WSS)/time-averaged WSS (TAWSS) around the tears, which could result in further wall splitting [11–19]. While more flow in the FL and high TAWSS are associated with expansion of the FL, less flow in the FL and low TAWSS are associated with thrombus formation and shrinkage of the FL during patient follow-up [12,16–19]. Regarding the impact of the tears, higher values of WSS have been detected for smaller distances between tears and also between tears and the aortic arch (AAr) [16, 18, 20]. Moreover, it was found that the presence of multiple tears has no impact on the TAWSS or flow patterns [14]. High relative residence time (RRT), i.e. the amount of time that a particle stays at a particular location, has been associated with thrombus formation in the patient follow-up, and is at its highest in the extremes of the FL, i.e. in the top and bottom of the FL [11, 19, 20]. In the study by Menichini [16], it was suggested that the involvement of major side branches could result in differences in TAWSS, flow patterns and therefore, in thrombus formation. The author also found that for larger branch-tear distances, higher TAWSS and more disturbed flows should be expected.

The aortic side branches (specially the minor ones) have been often excluded from the studied geometries in order to simplify them. However, the presence of both major and minor side branches has been suggested to change the flow patterns and haemodynamic parameters, which results in errors during thrombus estimation [16, 21]. Therefore, this thesis aims at studying the influence of the side branches on thrombus-related haemodynamic parameters in the FL of a TBAD. Hence, the importance of including side branches is assessed by analysing the haemodynamic differences between geometries with different side branches configuration to those of the geometry without side branches. Moreover, the effect of the number and location of the side branches in the FL on the thrombosis risk zones will be studied with the aim to gain insights in the influence of simplifications in the features of side branches that have their origin the FL.

2. Methodology

2.1. Geometry Extraction from CT Images

Geometrical information of a patient-specific aorta with TBAD was extracted from contrast-enhanced CT scans provided by the University Hospital of Düsseldorf. These CT scans were imported into the image segmentation software Mimics (Mimics v21.0, Materialize HQ, Leuven, Belgium), where 3D parts for the TL, FL, tears and aortic side branches were created (Fig. 1 and 2a). Dimensions and location of the aorta and tears were obtained and used as a starting point for the simplified model. Location, diameter and origin (from the TL or FL) of the side branches (minor and major) were also retrieved from the 3D model.

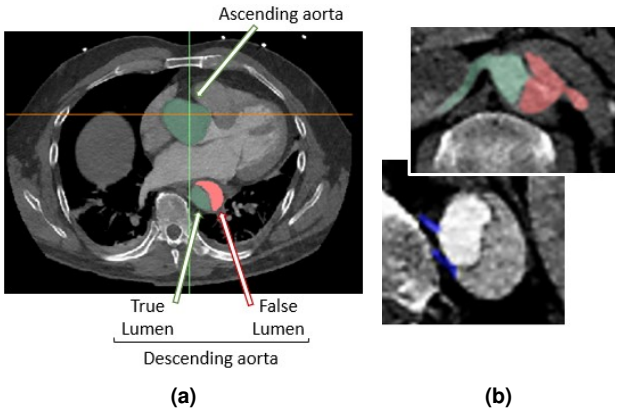

Fig. 1: Axial CT scans from a patient with TBAD. (a) TL and FL are identified in green and red, respectively. (b) In the top pannel, the renal arteries (which are two of the major aortic side branches) are with the colors of the TL or FL accordingly to their origin; In the bottom pannel, minor side branches are identified in blue.

2.2. Generation of Idealized Geometries

A total of 12 idealized 3D models of the descending aorta were created using SOLIDWORKS® (SOLIDWORKS 2017, Dassault Systèmes SOLIDWORKS Corp. HQ, Massachusetts, USA). The TL and FL were designed as straight tubes with a constant cross-section. The tears and side branches were designed with a circular shape of constant diameter. All side branches situated between the same two subsequent tears were clustered, leading to a maximum of 3 pairs of side branches, of which one originates from the TL and another from the FL. Their diameter was obtained through a modified Murray's law [19]. An extension of 5 cm was inserted at the inlet and all outlets, i.e. TL as well as the side branches, to overcome possible near-boundary effects

Two different sets of geometries were designed: G1-G7 with three tears where the branches configuration differ between the geometries and GA-GE with the same branches configuration but with two tears. G1 and G2 are compared in order to assess if including side branches leads to differences and then G1-G7 are also analysed to compare different side branches configurations. The other set, GA-GE is composed by geometries that only differ in the branch location (GA, GB and GC) or in number of branches (GA, GD and GE) in the FL, allowing to study the importance of these features. The idealized geometry G3 is shown in Fig. 2b where the tears diameters are depicted together with the side branches location.

2.3. Mesh Generation

Unstructured meshes (tetra/mixed type) were generated for all the geometries using the meshing software ICEM (ANSYS® ICEM CFD™ v14.5, Ansys Inc. HQ, Pennsylvania, USA). For each mesh, 3 layers of prism elements were generated at the aortic wall to allow better numerical calculations of the boundary layer [22]. In order to have a better discretization of the geometry, the Delaunay method was chosen and mesh refinement was applied [23].

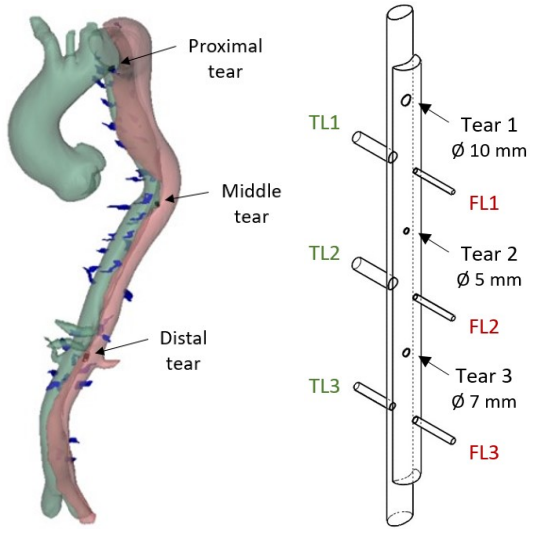

(a) (b)

Fig. 2: 3D geometry of the aorta and aortic branches from a patient with TBAD. (a) Reconstructed 3D part, with the tears indicated with arrows and TL, FL and side branches indicated with a colour code: green for TL and major side branches with the origin in the TL (celiac axis, superior mesenteric artery, right renal artery and the arteries originating from the aortic arch), red for FL and major side branches with the origin in this lumen (left renal artery) and blue for minor side branches. (b) Patient-inspired geometry G3 where the diameter (in mm) of each tear is presented next to it and the location of the branches is also depicted.

2.4. Boundary Conditions and Flow Models

For the CFD simulations, Fluent (ANSYS® Fluent v14.5, Ansys Inc. HQ, Pennsylvania, USA) was used. A transient analysis was adopted to allow the pulsatile behaviour of blood to be represented.

Regarding the boundary conditions, the vessel walls were assumed to be rigid with a no-slip condition. A spatially flat, but time-dependent velocity profile was specified at the TL inlet. This time-dependent profile was adapted from Fielden *et al.* [24] to match the TL area of the idealized geometry. Besides, the profile was adjusted to obtain a temporal mean velocity corresponding to the assumption that only 65% of the blood flow reaches the descending aorta [25]. The final velocity profile is shown in Fig. 3. An outflow condition was applied to all the outlets by using the following modified Murray's law [19]:

$$Outflow\ factor = \frac{Q_b}{Q_{in}} = \left(\frac{d_b}{d_{in}}\right)^2 \qquad (1)$$

where Q_b and Q_{in} indicate the flow rate in the branch and in the inlet, respectively. d_b and d_{in} are the diameters of the branch and of the inlet. As the TL and FL are not designed as circles, their diameter was defined using the hydraulic diameter [19]. The different features of the geometries used to compare the effect of using different branches configuration (G1-G7) are presented in Tab. 1. The location of the side branches is presented in Fig. 2b. As for the geometries used to analyse the influence of location and number of side branches (GA-GE), the total outflow from the involved side branches is 9.7% which is equally divided between the branches.

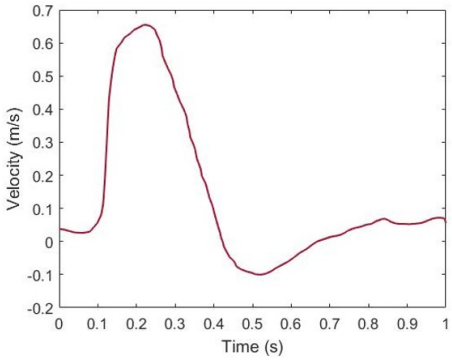

Fig. 3: Time-dependent velocity profile used as inlet boundary condition for the descending aorta: mean = 0.16 m/s; maximum = 0.66 m/s (at 0.22 s); minimum = -0.10 m/s (at 0.53 s). Adapted from Fielden *et al.* [24].

Tab. 1: Outflow percentage for each branch of the geometries with different side branches (SB) configuration (G1-G7). TL1, TL2 and TL3 correspond to branches with an origin in the TL and FL1, FL2 and FL3 to branches with an origin in the FL. The branch configuration of each geometry in presented in "SB included". The location of each branch is depicted in Fig. 2b.

Name	SB included	Outflow via SB (%)
G1	None	0.0
G2	TL1, TL2, TL3 FL2, FL3	31.5, 23.7, 8.0 6.8, 10.0
G3	TL1, TL2, TL3 FL1, FL2, FL3	23.0, 27.2, 9.2 4.6, 6.3, 9.7
G4	TL1, TL2, TL3 FL1	23.0, 35.9, 16.5 4.6
G5	TL1, TL2, TL3 FL3	31.0, 30.9, 6.8 11.3
G6	TL1, TL2, TL3	32.6, 32.5, 14.9
G7	FL1, FL2, FL3	25.2, 30.5, 24.3

The blood was treated as an incompressible and non-Newtonian fluid with a density of 1060 kg/m^3 [13]. The non-Newtonian behaviour was modelled using the Carreau model:

$$\mu = \mu_\infty + (\mu_0 - \mu_\infty)\left[1 + (\lambda\dot{\gamma})^2\right]^{\frac{n-1}{2}} \qquad (2)$$

where μ is the dynamic viscosity, $\dot{\gamma}$ is the shear rate, μ_∞ = 0.003 45 Pa s is the infinite-shear viscosity limit, μ_0 = 0.056 Pa s is the zero-shear viscosity limit, λ = 3.313 s is the time constant and n = 0.3568 is the dimensionless power-law index [26]. All of these values are blood-specific.

Freis *et al.* [27] found that in a healthy descending aorta, blood follows a laminar flow while in the ascending aorta it follows a turbulent flow. Although the AD changes the geometry features of the aorta, it was assumed that it will not have much influence, and so blood was modelled as laminar [11, 14, 16, 28].

2.5. Computation of Thrombosis Risk Factors

In order to achieve a periodic solution, all the simulations were run for three cardiac cycles before extracting the results. Values for TAWSS, RRT, time-averaged shear rate (TA$\dot{\gamma}$) and mass flow rate were

obtained in the post-processing stage with the aid of CFD Post (ANSYS® CFD Post v14.5, Ansys Inc. HQ, Pennsylvania, USA).

TAWSS allows to analyse the WSS magnitude over a cardiac cycle and is computed using Eq. 3 [29]:

$$TAWSS = \frac{1}{T}\int_0^T |WSS|\ dt \tag{3}$$

where WSS is the Wall Shear Stress and T is the period of a cardiac cycle. The scalar TA$\dot{\gamma}$ allows to analyse the shear rate magnitude over a cardiac cycle:

$$TA\dot{\gamma} = \frac{1}{T}\int_0^T |\dot{\gamma}|\ dt \tag{4}$$

A combined threshold of TAWSS < 0.2 Pa and TA$\dot{\gamma} < 50\,\mathrm{s}^{-1}$ was used to quantify the thrombosis risk zones due to low shear, as these values have been linked to thrombus formation [8, 16].

RRT is used to detect wall zones under both low and oscillatory shear stress and is calculated by following formulae [30]:

$$OSI = \frac{1}{2}\left(1 - \frac{\left|\int_0^T WSS\ dt\right|}{\int_0^T |WSS|\ dt}\right) \quad , \quad 0 \leq OSI \leq \frac{1}{2} \tag{5}$$

$$RRT = \frac{1}{(1 - 2 \cdot OSI) \cdot TAWSS} \tag{6}$$

where OSI represents the Oscillatory Shear Index, which is the frequency of change in orientation of the WSS vector relatively to the main flow direction.

A threshold of RRT $> 150\,\mathrm{Pa}^{-1}$ was used to quantify the thrombosis risk zones due to high residence time. As no clear threshold was found in literature, the threshold was chosen so that the differences in RRT in the FL of the different geometries became more evident for both extremes and between tears.

Areas were computed for the top and bottom of the FL for the low shear threshold and for these regions plus the regions between tears for the high RRT threshold. Area ratios were used for both parameters to allow a more direct comparison between geometries. Hence, areas for G2-G7 were divided by the correspondent G1 area. The procedure was repeated for GB-GE relatively to GA.

The mass flow rate ($\dot{Q}_m$) allows to compute the amount of flow that goes into and leaves from the FL:

$$\dot{Q}_m = \rho \cdot v_{avg} \cdot A \tag{7}$$

where ρ is the density of the fluid and v_{avg} is the average velocity that crosses the area A [31]. Inflow is considered as the flow going from the TL to the FL through a tear and *vice versa* for the outflow.

3. Results

A mesh- and step- sensitivity analysis was performed for G3 in order to obtain a both mesh size (around 2M elements) and time-step size (0.01 s) that is sufficiently small to allow accurate numerical results, but sufficiently large to be computed in a feasible time period [32]. For the other geometries, the same parameters were used.

3.1. Flow Patterns

No Branches versus With Branches: G1 vs G2

Instantaneous streamlines and velocity vectors at peak systole are shown in Fig. 4a and Fig. 4b for G1 and G2, respectively. The high velocity in the proximal tear results in evident disturbed flow with recirculation zones in the FL, above and below the tear, for both geometries. Both the streamlines and the velocity vectors show stronger recirculation with higher velocities for G2. During peak systole, the middle and distal tear function as re-entry tears as blood flows from the FL to the TL. Higher velocities are observed in the surrounding of these tears for G1 compared to G2. Moreover, almost no flow can be detected below the distal tear for G1 while a low velocity flow with no apparent recirculation is present between this tear and FL3 for G2.

During diastole (Fig. 4c and 4d), when there is backflow and the velocity is negative, the flux direction in the inlet and outlets is reversed. The result is a FL being supplied not only by the tears but also by the side branches in G2. Stronger recirculation is visible in the FL for G2 above the proximal tear and below the distal tear. Barely any recirculation is visible in the region where FL2 connects to the FL in G2.

3.2. Mass Flow Rate

Mass flow rate values for each tear are depicted in Fig. 5a for G1-G7 and in Fig. 5b for GA-GE.

Different Branches Configuration: G1-G7

Regarding G1-G7, the middle and distal tear do not function as re-entry tears for any of the geometries with side branches when using the cycle-averaged velocity (only inflow through these tears). High outflow through the proximal tear was obtained for most of the geometries which was found to take place in the proximal section of this tear while the inflow takes place in the distal portion (Fig. 6). Case G7 distinguishes from the others with a much higher inflow from all the tears with almost no outflow in the proximal tear. Moreover, the inflow through each tear is higher accordingly to the total predefined outflow via the involved side branches. Lower outflow through the proximal tear corresponds to geometries with proximal branches (G3, G4 and G7).

Location of Side Branch: GA, GB and GC

In Fig. 5b, none of the geometries has the distal tear functioning as a re-entry tear. Regarding GA, GB and GC, the outflow through the proximal tear increased with the distance of the branch to the tear (GB $<$ GA $<$ GC), while the inflow decreased with the distance (GB $>$ GA $>$ GC). The same was not obtained for the inflow through the distal tear.

Number of Side Branches: GA, GD and GE

The inflow obtained through the proximal tear for GA, GD and GE increased with the branch outflow near the tear. The outflow through this tear decreased with the outflow from the branch near the tear. The inflow through the distal tear is almost identical between GA, GD and GE, with GE having the highest value.

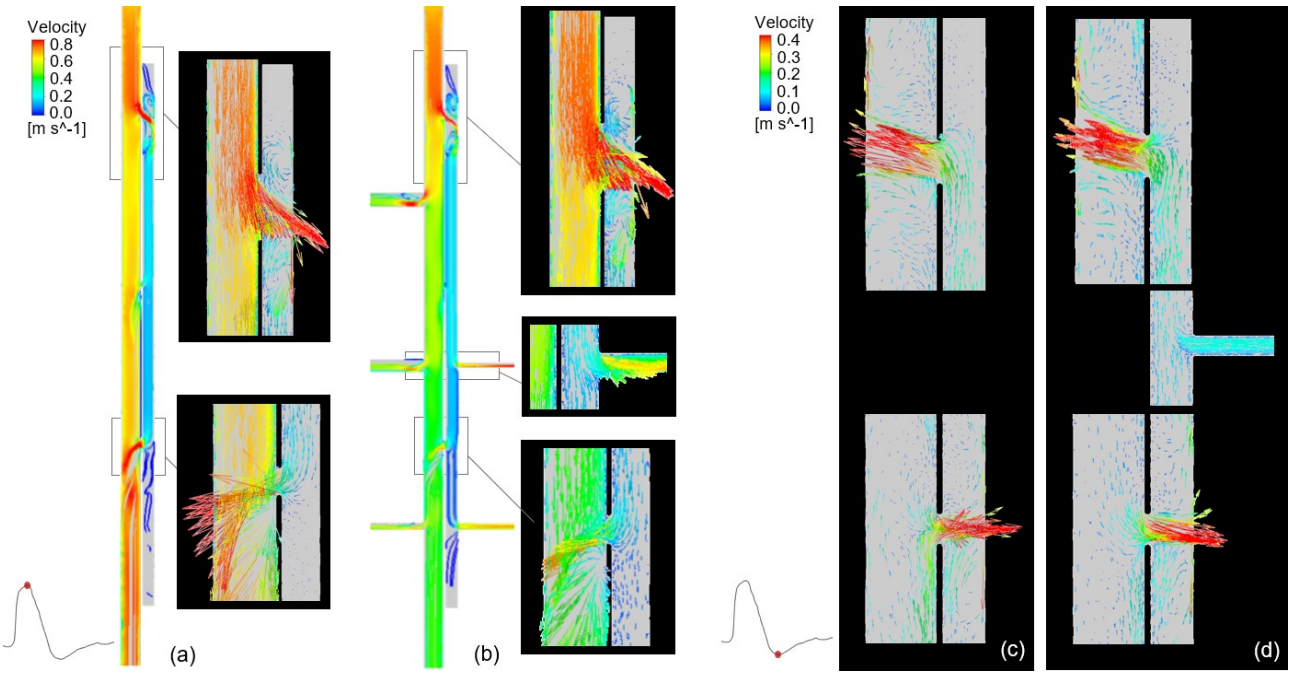

Fig. 4: 2D velocity streamlines and velocity vectors for the first and third tear during peak systolic velocity (at 0.22 s) in a cross-section of the frontal plane of (a) G1 and (b) G2, where the velocity vectors for the branch FL2 are also presented. Additionally, velocity vectors are presented for the same locations but during diastole at a minimum velocity of -0.10 m/s (at 0.52 s) for (c) G1 and (d) G2, where the velocity vectors for the branch FL2 are also presented for the middle side branch. Notice that the length of the vectors is merely a representation of the velocity magnitude. It does not mean that the flow is leaving the aorta through the aortic wall.

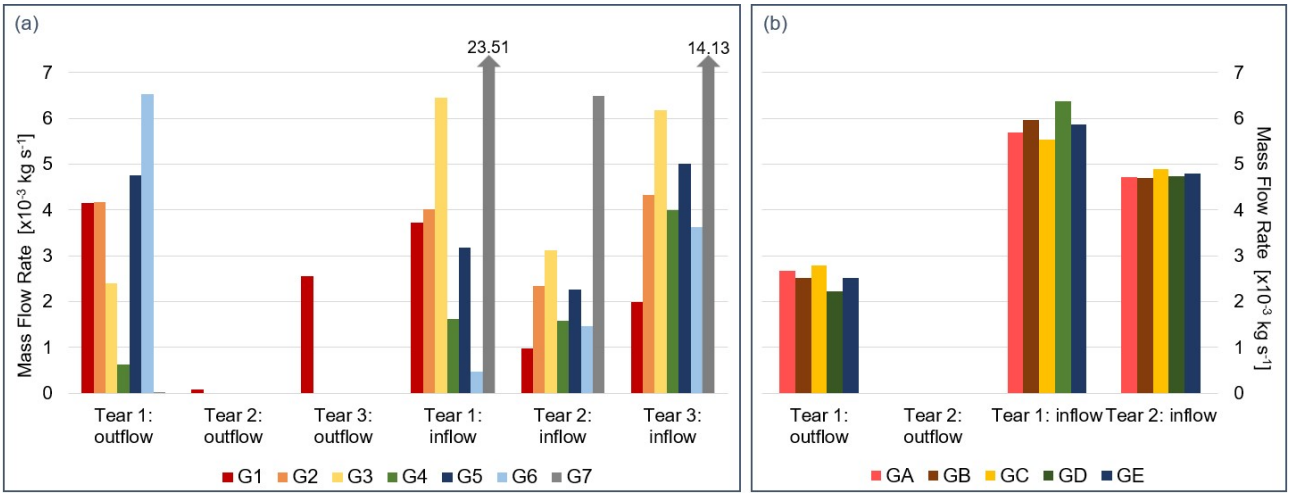

Fig. 5: Mass flow rate for each tear, where outflow means flow exiting the FL via each tear and inflow indicates that flow is entering the FL from the TL for (a) G1-G7 and (b) GA-GE. Notice that the mass flow rates for inflow through the proximal and distal tear are presented with arrows for G7 in (a) since these values are much larger than the others, allowing a better visualization for the user.

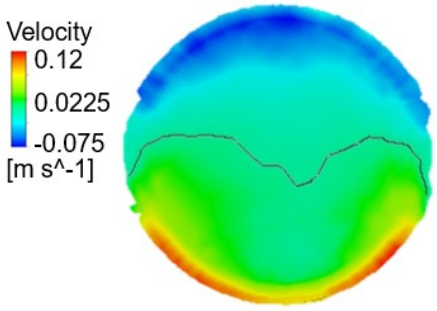

Fig. 6: Cycle-averaged velocities normal to the cross-section of the proximal tear of G1, where positive values represent flow towards the FL and negative values flow leaving the FL. The black line denotes a velocity equal to zero within the tear, where the velocity is negative above the line and positive below it.

3.3. Wall Haemodynamics: Qualitative Analysis

Different Branches Configuration: G1-G7

The tears are characterized by very high values of TAWSS (above 5 Pa) and large variations of TAWSS can be found in their surroundings (Fig. 7). Very low TAWSS values (below 0.2 Pa) are found in the top and bottom of the FL for G1-G6. Low values are also present in between tears, namely for G1 and above the most proximal branch of G2 and G5. Higher TAWSS just below the distal tear characterizes the geometries with a distal branch (in the position FL3). For G7, a low TAWSS region can be found at the bottom of the FL, while high TAWSS regions are spread over the whole FL.

As shown in Fig. 8, the top and bottom of the FL are

characterized by RRT values around $200\,\mathrm{Pa}^{-1}$ for G1-G6. Similar to the findings for TAWSS but inversely proportional, the high-RRT zone of G7 can only be found at the bottom of the FL. For geometries with a distal branch, the high-RRT zones begin below this branch, while for the other geometries, it starts below the distal tear. These high values of RRT are also visible between the proximal and middle tear for G1 and G2. At the top of the FL, high variability is visible within the different geometries. Small seldom high-RRT zones - "hotspots" - are also visible around the tears for G1-G6.

Location of Side Branch: GA, GB and GC

In Fig. 9, the highest TAWSS values in the FL are here as well obtained in the tears and in their surroundings. Regarding GA-GC, slightly higher TAWSS values were obtained for GB in the distal tear compared to the GA and GC. Higher TAWSS were observed below the branch closest to the FL bottom for each geometry. Lower values TAWSS-values were obtained above the branch closest to the FL top for GA and GC.

No clear differences are visible for the values of RRT below the distal tear of GA-GC in Fig. 10. For all the geometries, "hotspots" are visible in the surroundings of the involved side branches and/or tears. In between tears, GB has lower RRT values than GA and GC, which have higher values between the proximal tear and branch in particular. At the top of the FL, the high-RRT zone shrinks with the distance to the involved side branch.

Number of Side Branches: GA, GD and GE

In Fig. 9, lower values of TAWSS are obtained between the branches of GD and between the proximal and middle branch of GE compared to GA.

The RRT increases in between tears with the number of branches for GA, GD and GE. At the top of the FL, the largest high-RRT zone corresponds to GD (Fig. 10). No clear differences are visible for the values of RRT below the distal tear of these geometries.

3.4. Wall Haemodynamics: Quantitative Analysis

The ratio of areas that fulfill the pathological low shear threshold and the threshold of high residence time is depicted in Tab. 2 for GB-GE relatively to GA. This is done for different regions of the FL limited by the tears and/or the top/bottom of the FL. The pathological low shear areas for GA-GE are similar between all cases in the FL extremes (ratio of $[0.97,1.02]$).

Location of Side Branch: GA, GB and GC

A larger area of pathological RRT was obtained for a smaller distance of the branch to the top of the FL between GA, GB and GC. At the bottom of the FL, no similar relationship could be observed with GC having the largest area followed by GB and only then by GA. As for the region in between tears, the areas reflect the presence of "hotspots" near the branches and/or tears. Here, GB has almost a null area and GA has the largest. The latter are between the proximal tear and the branch (Fig. 10a).

Number of Side Branches: GA, GD and GE

Regarding GA, GD and GE, a much larger area of $\mathrm{RRT} > 150\,\mathrm{Pa}^{-1}$ was obtained for GD at the top of the FL (2.24 times the area of GA) while GE has a smaller area. Both geometries with distal branches have an identical area below the distal tear, which is slightly higher compared to GA (ratio of $[1.09, 1.11]$). The thrombosis-risk RRT area between tears increased with the number of branches, with GE showing a very large area between its branches which is also visible in Fig. 10e.

4. Discussion

As partial thrombosis is linked with poor long term patient outcomes, prediction of thrombus-prone zones might be very helpful [5, 6]. However, it has been shown that not including (major and minor) side branches leads to discrepancies in thrombus estimation in these models [16, 21].

Multiple idealized geometries with different side branches configuration were designed based on the aorta of a TBAD patient. Thrombus-related haemodynamic parameters were retrieved for each geometry to investigate the influence on several thrombosis related parameters. The same was performed for idealized geometries that only differ in the location or number of involved side branches.

Different Branches Configuration: G1-G7

High shear stress ($\mathrm{TAWSS} > 5\,\mathrm{Pa}$) is associated with platelet activation [8]. Our study showed that values above $5\,\mathrm{Pa}$ were found at the tears, which suggests that platelets might get activated in the tears and therefore, a higher inflow into the FL should allow more activated platelets to reach this lumen. High variations in the flow rate at these tears were obtained for the different geometries, where geometries with branches often have higher tear inflow than the one without (G1).

Low shear stresses ($\mathrm{TAWSS} < 0.4\,\mathrm{Pa}$) are associated with thrombus development and platelet adhesion [29]. The presence of low shear zones at the top and bottom of the FL should allow, not only low-shear induced thrombosis, but also that the high-shear activated platelets coming from the tears adhere to the wall in these regions and form thrombus [33].

The stronger recirculation visible in the flow pattern analysis at the top of the FL for G2 resulted in smaller high-RRT zones in G2 compared to G1. A high RRT has been associated to thrombus development due to cell-cell and cell-wall interactions, making it more likely that more thrombus will be formed in these regions for G1 compared to G2 [18, 19, 34].

The small shear differences obtained for the different geometries suggest that the shear is not highly dependent on the geometry unless for extreme cases such as G7.

An increase of the inflow through tears distal to the involved side branch was observed for G4, which suggests that the blood will move upwards to supply this branch. This could mean that if a TEVAR treatment

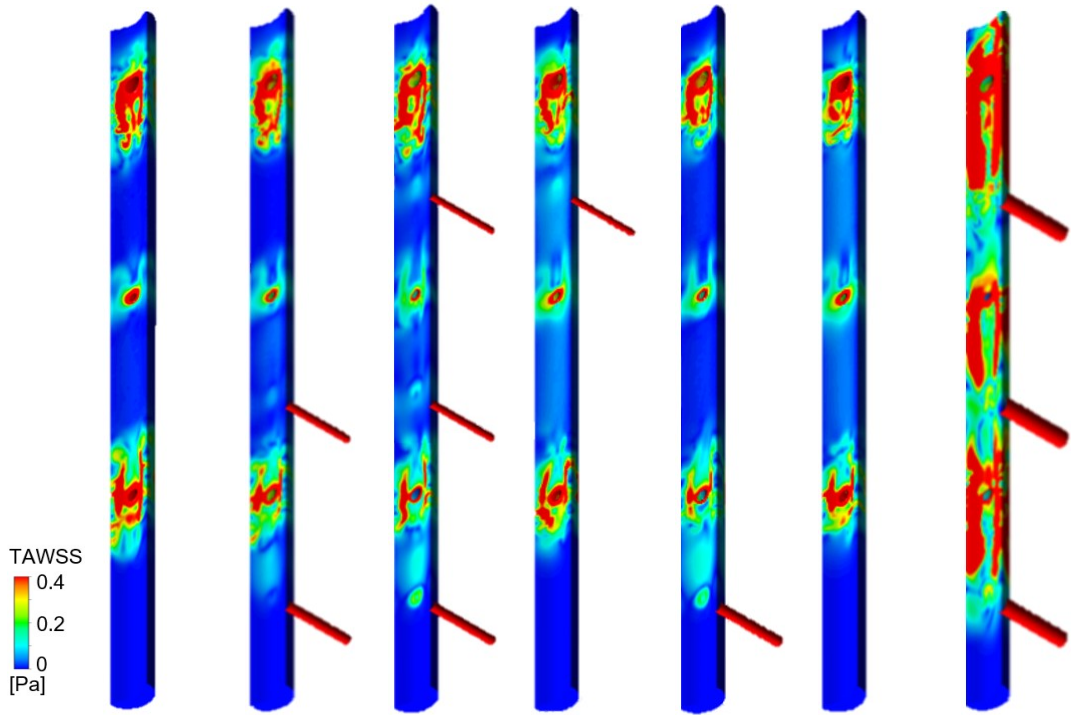

Fig. 7: Cycle-averaged wall shear stress (TAWSS) for the geometries (G1-G7) at the FL portion of the wall near the tears.

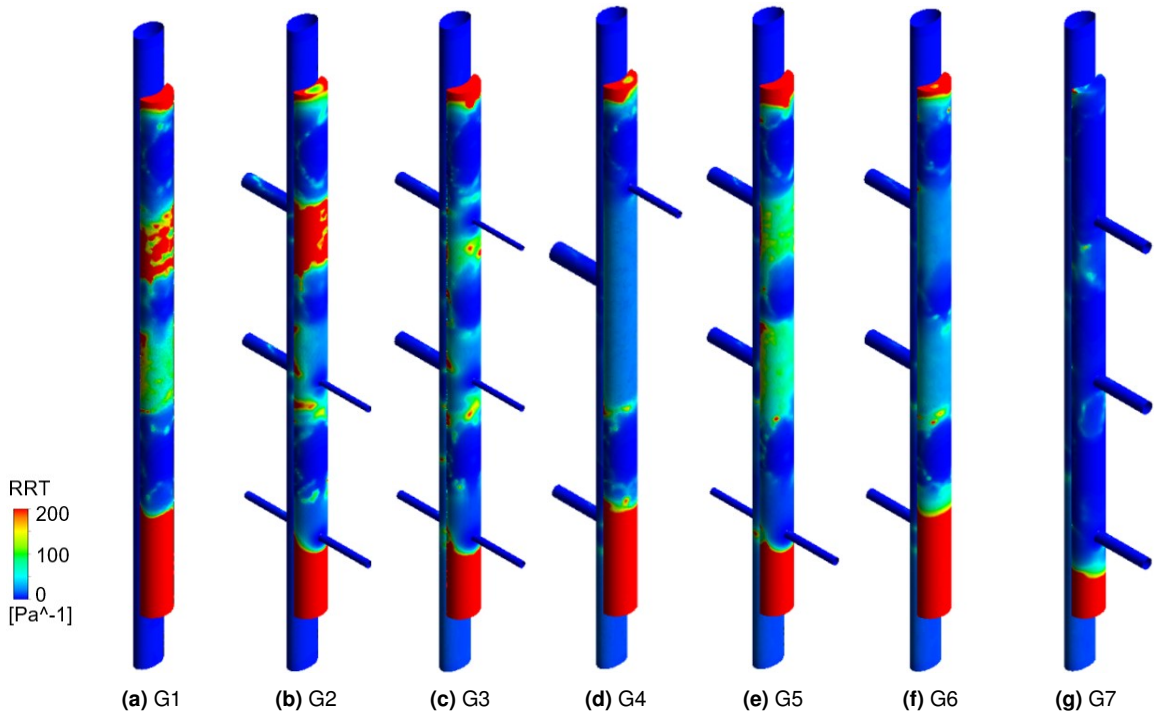

Fig. 8: RRT for the different geometries (G1-G7) at the portion of the wall opposite to the tears.

leaves a distal tear open and there is a an involved side branch located above this tear, it might happen that this tear will supply the branch. This could lead to an increase in the flow and thus, decreasing thrombus formation in the region above the tear. This results in a patent or partial thrombosed FL, which are associated to higher mortality than complete thrombosis [5].

Overall, the results suggest that the presence of involved side branches influences the FL thrombus-related haemodynamics, in particular the RRT, and therefore the thrombus estimation. Moreover, the estimation of the thrombosis risk zones depends on the different branches configuration as over- or underestimation of thrombus formation was obtained in different regions of the FL for the geometries with branches compared to the geometry without branches.

Location of Side Branch: GA, GB and GC

Geometries that have a proximal branch (such as GB) are characterized with less “hotspots”, meaning that less stagnation zones are expected to be found in

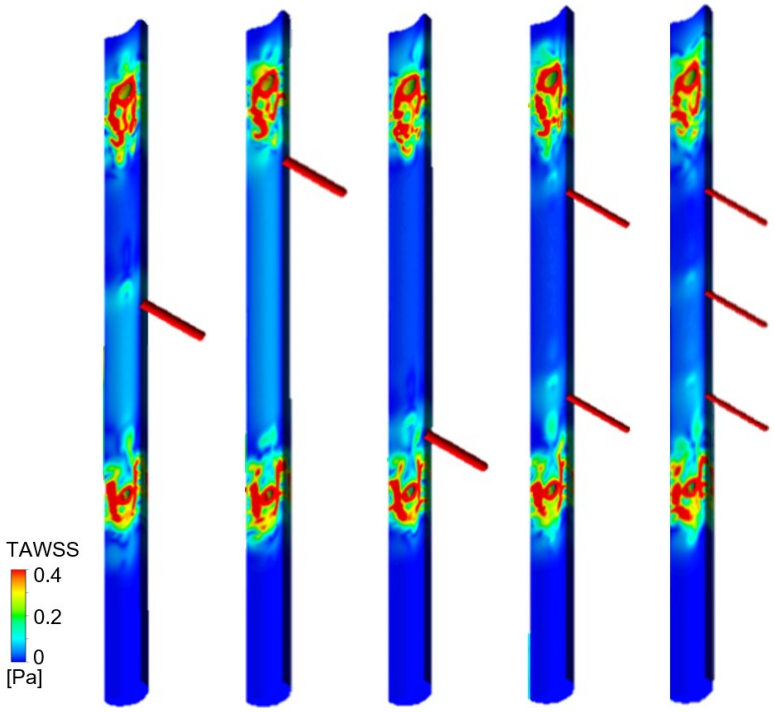

Fig. 9: Cycle-averaged wall shear stress (TAWSS) for the geometries (GA-GE) at the FL portion of the wall near the tears.

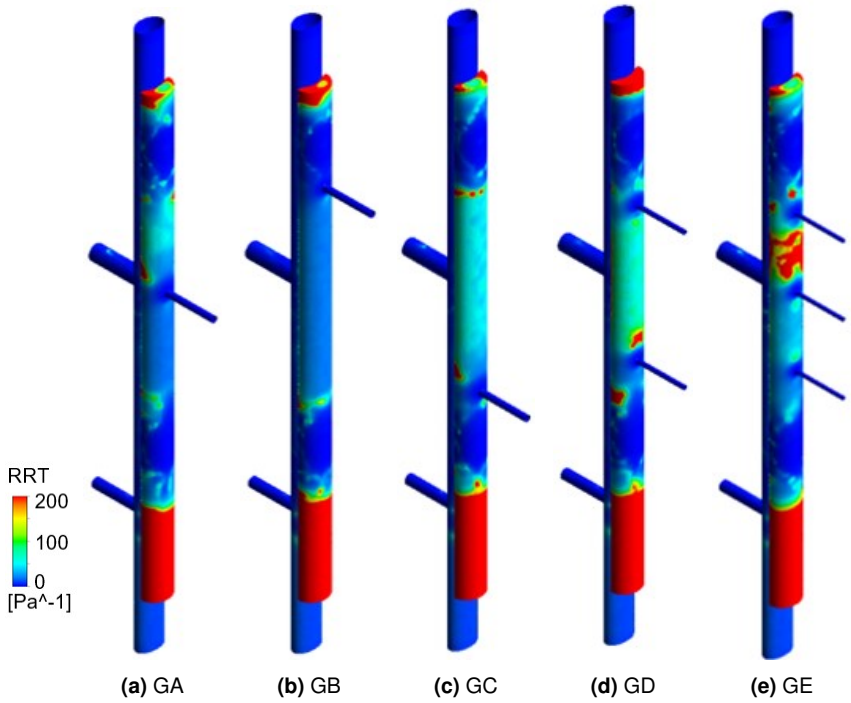

Fig. 10: RRT for the different geometries (GA-GE) at the portion of the wall opposite to the tears.

the FL of this geometry and therefore less thrombus should be formed in between the tears.

A slightly higher inflow into the FL was obtained for the tear near the branch for both GB and GC, suggesting that the tear will supply the branch. Lower inflow was obtained for the tear further away from the branch. The differences were, however, more evident for the tear closer to the AAr.

Larger critical RRT areas were obtained at the top of the FL with a proximal side branch. The proximity of a branch to a tear seems to redirect the flow into the branch, decreasing the amount of flow in the top of the FL, expanding the thrombosis risk area in this region. The same was obtained for the distal tear and the bottom of the FL. The thrombosis risk zone near the proximal tear decreased with the tear-branch distance, which is in accordance with what was suggested by Menichini [16]. However, this was not obtained when considering the distal tear.

Based on these observations, the distance between AAr and the branch seems to have an impact on the thrombosis risk zones estimation.

Tab. 2: Ratio of the areas obtained for each region of the FL that fulfills the conditions for TAWSS & TA$\dot{\gamma}$ (TAWSS lower than 0.2 Pa and TA$\dot{\gamma}$ lower than 50 s^{-1}) . The areas for the regions that fulfill the RRT higher than 150 Pa^{-1} threshold are given as well.

		Area Ratio		
		Above t1	**Between t1 and t2**	**Below t2**
GB	TAWSS & TA$\dot{\gamma}$	0.97	-	1.00
	RRT	1.56	0.16	1.11
GC	TAWSS & TA$\dot{\gamma}$	1.02	-	1.00
	RRT	0.78	0.51	1.14
GD	TAWSS & TA$\dot{\gamma}$	1.00	-	1.00
	RRT	2.24	1.16	1.09
GE	TAWSS & TA$\dot{\gamma}$	0.97	-	0.98
	RRT	0.65	2.23	1.11

Number of Side Branches: GA, GD and GE

By changing the number of branches, the outflow and location of each side branch also varies, which presents a limitation to this comparison.

For the same location of a proximal branch, a larger high-RRT zone was obtained at the top of the FL for a proximal side branch with a higher outflow. A sufficiently large outflow via the branch might be required to help redirecting the flow into the branches, otherwise it just leads to an increase in the inflow of blood which can result in higher velocities above the proximal tear, shrinking the high-RRT zone.

The presence of several branches in between tears seems to induce a disturbed flow between neighbouring branches. Higher RRTs between the tears were found for geometries with a higher number of branches in the FL and can, therefore, be associated with more thrombus development between consecutive tears.

The difference in outflow from the distal branch between GD and GE does not seem to affect the thrombosis risk zone in this area, in contrast to what was obtained at the top of the FL. This supports the previous observations that the proximity of the tears and branches to the AAr affects the results, with the smaller the branch-AAr distance, the more relevant the impact of the side branches.

Limitations and Future Work

In order to guarantee that the solver converges to accurate results, a sensitivity analysis is required for each geometry [32]. However, it was only performed for one geometry and generalized for the others, not assuring proper mesh and step sizes for each geometry. A mesh and step-size sensitivity analysis should be performed for each geometry in future works.

It should be noticed that the geometries used in this paper are simplified as no curvature, aortic arch or variable aortic diameter is included. Besides, the side branches were simplified by clustering them, inserting them in the middle point between the tears (for G1-G7) and modelling them in parallel to each other and perpendicular to the centreline of the FL. These approximations are expected to influence the flow patterns and haemodynamic parameters and thus, to influence the thrombosis risk zones estimation [13, 17]. A study with a more realistic, patient-specific geometry should, therefore, be performed where all the side branches from the aorta should also be included in the reconstructed geometry.

The prediction of the thrombosis risk zones was based on haemodynamic parameters, with a qualitative interpretation dependent on the scale used and a quantitative comparison dependent on the values defined for the thresholds. The results of this study suggest that the RRT is better than shear parameters when investigating the impact of the branches. Furthermore, a validation of the results is need, to really draw well-founded conclusions on which parameters is the best. As a future step, the results of this thesis should be compared with those obtained with a thrombosis model such as the one created by Menichini [16].

5. Conclusions

In this research, the influence of involved side branches in a TBAD was analysed by comparing the thrombosis risk zones obtained based on different haemodynamic parameters for multiple idealized geometries that differ regarding the branches features.

It was found that a smaller tear-branch distance leads to larger thrombosis risk zones, in particular when they are located proximally. The outflow via the side branch also appears to be relevant for the estimation of these zones. Moreover, involved branches can indeed lead to over- or underestimation of thrombosis risk zones when not included in the model. Therefore, they should be considered by both doctors and engineers in following studies on this disease in order to obtain a more adequate thrombosis estimation, which will help to predict the patient outcome.

6. Acknowledgments

This document was written and made publicly available as an institutional academic requirement and as a part of the evaluation of the MSc thesis in Biomedical Engineering of the author at Instituto Superior Técnico. The work described herein was performed at bioMMeda, the research group on Biofluid, Tissue and Solid Mechanics for Medical Applications of

Ghent Univesity (Ghent, Belgium), during the period February-September 2019, under the supervision of Prof. Patrick Segers, and within the frame of the Erasmus programme. The thesis was co-supervised at Instituto Superior Técnico by Prof. Paulo Fernandes.

References

[1] Melvinsdottir I. H., Lund S. H., Agnarsson B. A., Sigvaldason K., Gudbjartsson T., and Geirsson A., "The incidence and mortality of acute thoracic aortic dissection: results from a whole nation study," *European Journal of Cardio-Thoracic Surgery*, vol. 50, pp. 1111–1117, 06 2016.

[2] Cherry K. J. and Dake M. D., "Chapter 31 - aortic dissection," in *Comprehensive Vascular and Endovascular Surgery (Second Edition)* (Hallett J. W., Mills J. L., Earnshaw J. J., Reekers J. A., and Rooke T. W., eds.), pp. 517 – 531, Philadelphia: Mosby, second edition ed., 2009.

[3] Tsai T. T., Evangelista A., Nienaber C. A., Myrmel T., Meinhardt G., Cooper J. V., Smith D. E., Suzuki T., Fattori R., Llovet A., Froehlich J., Hutchison S., Distante A., Sundt T., Beckman J., Januzzi J. L., Isselbacher E. M., and Eagle K. A., "Partial thrombosis of the false lumen in patients with acute type b aortic dissection," *New England Journal of Medicine*, vol. 357, no. 4, pp. 349–359, 2007.

[4] Zhou Y., Wang W.-C., Zhang X.-M., Yang C., Zheng J., Yang L., Dong L., Hu X., Zhu T., Wang Y.-L., and Yang Y., "Aortic remodelling after thoracic endovascular aortic repair for acute and subacute type b aortic dissection," *Quantitative Imaging in Medicine and Surgery*, vol. 8, no. 4, 2018.

[5] Li D., Ye L., He Y., Cao X., Liu J., Zhong W., Cao L., Zeng R., Zeng Z., Wan Z., and Cao Y., "False Lumen Status in Patients With Acute Aortic Dissection: A Systematic Review and Meta-Analysis," *Journal of the American Heart Association*, vol. 5, 05 2016.

[6] Uchida T. and Sadahiro M., "Thoracic endovascular aortic repair for acute aortic dissection," *Annals of vascular diseases*, vol. 11, no. 4, p. 464–472, 2018.

[7] Colman R., Marder V., Clowes A., George J., and Goldhaber S., *Hemostasis and Thrombosis: Basic Principles and Clinical Practice*. Philadelphia, Pennsylvania: Lippincott Williams and Wilkins, 5th ed., 2006.

[8] Hathcock J., "Flow effects on coagulation and thrombosis," *Arteriosclerosis, thrombosis, and vascular biology*, vol. 26, pp. 1729–37, 09 2006.

[9] Lowe G. D. O., "Factor ix and thrombosis," *British Journal of Haematology*, vol. 115, no. 3, pp. 507–513, 2001.

[10] Yesudasan S. and Averett R. D., "Recent advances in computational modeling of thrombosis," 2018.

[11] Chen D., Müller-Eschner M., von Tengg-Kobligk H., Barber D., Böckler D., Hose R., and Ventikos Y., "A patient-specific study of type-B aortic dissection: evaluation of true-false lumen blood exchange," *BioMedical Engineering OnLine*, vol. 12, no. 1, 2013.

[12] Cheng Z., Tan F. P. P., Riga C. V., Bicknell C. D., Hamady M. S., Gibbs R. G. J., Wood N. B., and Xu X. Y., "Analysis of Flow Patterns in a Patient-Specific Aortic Dissection Model," *Journal of Biomechanical Engineering*, vol. 132, 03 2010. 051007.

[13] Tse K. M., Chiu P., Lee H., and Ho P., "Investigation of hemodynamics in the development of dissecting aneurysm within patient-specific dissecting aneurismal aortas using computational fluid dynamics (cfd) simulations," *Journal of biomechanics*, vol. 44, pp. 827–36, 03 2011.

[14] Wan N., Ganesan P., Sun Z., Osman K., and Einly L., "The impact of the number of tears in patient-specific stanford type b aortic dissecting aneurysm: Cfd simulation," *Journal of Mechanics in Medicine and Biology*, vol. 14, 11 2013.

[15] Karmonik C., Partovi S., Müller-Eschner M., Bismuth J., Davies M., Shah D., Loebe M., Böckler D., Lumsden A., and Von Tengg-Kobligk H., "Longitudinal computational fluid dynamics study of aneurysmal dilatation in a chronic debakey type iii aortic dissection," *Journal of vascular surgery*, vol. 56, pp. 260–3.e1, 05 2012.

[16] Menichini C., *Mathematical Modelling of Thrombus Formation in Type B Aortic Dissection*. London, United Kingdom: Imperial College London, 2018.

[17] Ahmed S. B., Dillon-Murphy D., and Figueroa C., "Computational study of anatomical risk factors in idealized models of type b aortic dissection," *European Journal of Vascular and Endovascular Surgery*, vol. 52, no. 6, pp. 736 – 745, 2016.

[18] Cheng Z., Riga C., Chan J., Hamady M., Wood N. B., Cheshire N. J., Xu Y., and Gibbs R. G., "Initial findings and potential applicability of computational simulation of the aorta in acute type b dissection," *Journal of Vascular Surgery*, vol. 57, no. 2, Supplement, pp. 35S – 43S, 2013. Beyond Borders.

[19] Xu H., Piccinelli M., Leshnower B. G., Lefieux A., Taylor W. R., and Veneziani A., "Coupled morphological–hemodynamic computational analysis of type b aortic dissection: A longitudinal study," *Annals of Biomedical Engineering*, vol. 46, pp. 927–939, 2018.

[20] Tang A., Fan Y., Cheng S., and Chow K., "Biomechanical factors influencing type b thoracic aortic dissection: Computational fluid dynamics study," *Engineering Applications of Computational Fluid Mechanics*, vol. 6, no. 4, pp. 622–632, 2012.

[21] Zhang Y., Lu Q., Feng J., Yu P., Zhang S., TengZ. abd Gillard, J., Song R., and Jing Z., "A pilot study exploring the mechanisms involved in the longitudinal propagation of acute aortic dissection through computational fluid dynamic analysis," *Cardiology*, vol. 128, no. 2, pp. 220–225, 2014.

[22] Zbigniew T., Obidowski D., Reorowicz P., Stefańczyk L., Fortuniak J., and Jozwik K., "Numerical simulations of the pulsatile blood flow in the different types of arterial fenestrations: Comparable analysis of multiple vascular geometries," *Biocybernetics and Biomedical Engineering*, vol. 38, 02 2018.

[23] ANSYS I., "Ansys icem cfd user manual 2012." Availabe at: `https://pdfs.semanticscholar.org/c728/37a63921bbc47c83fa3d6bad8e2d9a86e2f7.pdf`, Last accessed on 2019-08-7.

[24] Fielden S., Fornwalt B., Jerosch-Herold M., Eisner R., Stillman A., and Oshinski J., "A new method for the determination of aortic pulse wave velocity using cross-correlation on 2 d pcmr velocity data," *Journal of magnetic resonance imaging : JMRI*, vol. 27, pp. 1382–7, 06 2008.

[25] Benim A., Nahavandi A., Assmann A., Schubert D., Feindt P., and Suh S., "Simulation of blood flow in human aorta with emphasis on outlet boundary conditions," *Applied Mathematical Modelling*, vol. 35, no. 7, pp. 3175 – 3188, 2011.

[26] Molla M. and Paul M., "Les of non-newtonian physiological blood flow in a model of arterial stenosis," *Medical engineering and physics*, vol. 34, pp. 1079–87, 12 2011.

[27] Freis E. D. and Heath W. C., "Hydrodynamics of aortic blood flow," *Circulation Research*, vol. 14, no. 2, pp. 105–116, 1964.

[28] Zhang C., Xie S., Li S., Pu F., Deng X., Fan Y., and Li D., "Flow patterns and wall shear stress distribution in human internal carotid arteries: The geometric effect on the risk for stenoses," *Journal of Biomechanics*, vol. 45, no. 1, pp. 83 – 89, 2012.

[29] Nobili M., Sheriff J., MorbiducciU., R. A., and Bluestein D., "Platelet activation due to hemodynamic shear stresses: damage accumulation model and comparison to in vitro measurements," *ASAIO journal (American Society for Artificial Internal Organs)*, vol. 54, no. 1, 2008.

[30] Himburg H. A., Grzybowski D. M., Hazel A. L., LaMack J. A., Li X.-M., and Friedman M. H., "Spatial comparison between wall shear stress measures and porcine arterial endothelial permeability," *American Journal of Physiology-Heart and Circulatory Physiology*, vol. 286, no. 5, pp. H1916–H1922, 2004.

[31] McBride E., "Mass and energy analysis of control volumes," 2018. Availabe at: `https://slideplayer.com/slide/13312349/`. Last accessed on: 2019-09-15.

[32] ANSYS I., "Ansys fluent 12.0 user's guide." Availabe at: `http://www.afs.enea.it/project/neptunius/docs/fluent/html/ug/node980.htm`, Last accessed on 2019-08-4.

[33] Boreda R., Fatemi R., and Rittgers S., "Potential for platelet stimulation in critically stenosed carotid and coronary arteries," *J Vasc Invest*, vol. 1, p. 26–37, 1995.

[34] Hoi Y., qing Zhou Y., Zhang X., Henkelman R. M., and Steinman D. A., "Correlation between local hemodynamics and lesion distribution in a novel aortic regurgitation murine model of atherosclerosis," *Annals of Biomedical Engineering*, vol. 39, pp. 1414–1422, 2011.